SCIENCE CHINA
Chemistry

• ARTICLES •
· SPECIAL TOPIC · Electrochemical Power Sources

December 2017 Vol.60 No.12:1554–1560
doi: 10.1007/s11426-017-9123-0

Structurally modulated Li-rich cathode materials through cooperative cation doping and anion hybridization

Xu-Dong Zhang[1,2], Ji-Lei Shi[1,2], Jia-Yan Liang[1,2], Ya-Xia Yin[1,2*], Yu-Guo Guo[1,2*] & Li-Jun Wan[1,2]

[1]*CAS Key Laboratory of Molecular Nanostructure and Nanotechnology, CAS Research/Education Center for Excellence in Molecular Sciences, Institute of Chemistry, Chinese Academy of Sciences, Beijing 100190, China*
[2]*School of Chemistry and Chemical Engineering, University of Chinese Academy of Sciences, Beijing 100049, China*

Received July 4, 2017; accepted August 16, 2017; published online November 20, 2017

High capacity Li-rich materials are mighty contenders for building rechargeable batteries that coincide with the demand in energy density. Fully realizing the extraordinary capacity involves oxygen evolution and related cation migration, resulting in phase transitions and deteriorations that would hinder their practical application. In an attempt to enhance the anodic redox participation and stabilize the structure at the same time, we proposed a structural modulation strategy with modification on anion hybridization intensifying and cation doping. Spectator ions with large ionic radius were introduced into the lattice during calcination with stannous chloride and the d-p hybridization between transition metal 3d and oxygen 2p orbitals was subsequently intensified along with expelling weakly bonded chloride species in the reheating process. Both of the reversible capacity and stability upon cycling were remarkably improved through the cooperation of bond alteration and dopant. This strategy might provide new insight into the modulation of the structure to truly fulfill the potential of Li-rich materials.

Li-ion batteries, cathode materials, structural modification, doping, anodic redox

Citation: Zhang XD, Shi JL, Liang JY, Yin YX, Guo YG, Wan LJ. Structurally modulated Li-rich cathode materials through cooperative cation doping and anion hybridization. *Sci China Chem*, 2017, 60: 1554–1560, doi: 10.1007/s11426-017-9123-0

1 Introduction

Over the past two decades, enormous successes have been created in information globalization and livelihood convenience with the help of capable portable electronics powered by the state-of-the-art lithium ion batteries (LIBs) [1–3]. Moreover, it is also LIBs that we have chosen as the choice for powering the electric vehicle (EV), plug-in hybrid electric vehicle (PHEV) and grid energy storage [4,5]. Along with the popularization of applications comes a demand for better rechargeable batteries with higher energy density, in which lack of cathode materials becomes the main bottleneck [5–7]. Motivated by the pursuit of higher energy density, extensive investigations have been made on lithium and manganese rich (Li-rich) $x\mathrm{Li_2MnO_3}\cdot(1-x)\mathrm{LiMO_2}$ (M=Ni, Co and Mn) materials. Due to capacity over 250 mA h g^{-1}, this kind of material is considered as a promising contender for the next generation cathode material following layered materials with high nickel content [8,9].

Li-rich materials are inclined to be described as composites of two phases, the rhombohedral $R\bar{3}m$ phase $\mathrm{LiMO_2}$ and monoclinic $C2/m$ phase $\mathrm{Li_2MnO_3}$ intimately integrated and interconnected at nanoscale [10–12]. The extraordinary capacity originates from the $\mathrm{Li_2MnO_3}$ component, which stabilizes $\mathrm{LiMO_2}$ at fully delithiated state by its structural compatibility with rhombohedral phase and further affords sites for the lithium intercalation after electrochemically

---

*Corresponding authors (email: yxyin@iccas.ac.cn; ygguo@iccas.ac.cn) or chemically activation. This activation involves lithium extraction and concomitant oxidation of oxygen ions. To explain the oxygen evolution, oxygen loss from the surface accompanied with scenarios including transition metal (TM) migration from surface to bulk, electrolyte decomposition and phase transformation to spinel-like has been proposed, but the released oxygen gas still could not compensate the charge of lithium extraction [13–16]. Recently reported reversible anodic oxygen oxidation ($O^{2-}\rightarrow O_2^{2-}$) may complement the mechanism of oxygen evolution [17–19]. For $Li_2Ru_{1-y}Sn_yO_3$ anion participates in the redox reaction with the assistance of the d-sp hybridization associated with a reductive coupling from Ru. However the oxidation of tetravalent cation is absent in common Li-rich materials composed of 3d elements Ni, Co and Mn [17,20]. Therefore, increasing the TM–O bond covalence should be an interesting strategy to fully realize the potential of common Li-rich materials [2,21].

Another issue that impedes the practical application of Li-rich materials is the phase transitions inducing severe capacity deterioration and voltage decay during prolonged cycling [22,23]. The deintercalation of vast majority of Li ions from Li-rich material at the end of charge triggers transition metal migrating from octahedral sites in the TM slab to octahedral sites in the Li slab as aforementioned, meanwhile some of the cations may be trapped in the intermediary tetrahedral sites. The structural transition (from layered to spinel-like phase) resulting from such trapping incurs the voltage decay [24]. Further cation rearrangements lead to $Fm\bar{3}m$ rock-salt structure on the surface, which is detrimental to the capacity retention due to the absence of lithium ion diffusion path in the lattice [25,26]. Doping electrochemically inactive spectator ions with large ionic radius was demonstrated to be an effective method to obviate the phase transitions issue [23,24,27].

Herein, we report a simple and effective strategy to modify Li-rich material with the formula of $0.5Li_2MnO_3\cdot 0.5LiNi_{1/3}Co_{1/3}Mn_{1/3}O_2$ by calcination with metal chloride and then washing-reheating. The spectator metal ions and weakly bonded chloride were penetrated into the lattice during the first calcination, and then the TM–O bond covalence was enhanced along with the chloride species removal in the following rinse and reheating. Owing to the raised anodic participation caused by hybridization intensifying, the modified material exhibited high reversible capacity of 288 mA h g^{-1} at 0.05 C while the pristine material only showed 249 mA h g^{-1}. This strategy not only raised the anodic redox but also simultaneously suppressed the phase transition via cation doping, consequently improved the stability during prolonged cycling with capacity retention of 91.5% after 100 cycles at 0.2 C and mitigated the voltage decay from 365 to 279 mV. These improvements make the modified Li-rich material much more appealing for practical application.

2 Experimental

2.1 Samples preparation

The carbonate precursors were prepared via carbonate co-precipitation method with the ratio of Ni:Co:Mn at 1:1:4. To prepare pristine Li-rich material, the as-prepared carbonate precursors with an appropriate amount of Li_2CO_3 (5% excess) were calcined at 450 °C for 5 h and 820 °C for 12 h in air, after naturally cooled to room temperature pristine $Li_{1.2}Ni_{0.13}Mn_{0.13}Mn_{0.54}O_2$, denoted as PLR hereafter, was obtained.

To prepare cation doped and anion hybridization intensified Li-rich material, the carbonate precursors were calcined with Li_2CO_3 and moderate $SnCl_2\cdot 2H_2O$ (Sn:M=0.0375 in molar ratio) at 450 °C for 5 h and 820 °C for 12 h in air, after naturally cooled to room temperature the powders were washed by pure water and oven-dried at 80 °C overnight. Finally, the dried powders were re-calcined at 700 °C for 6 h in air to remove chloride species and get the modified $Li_{1.2}Ni_{0.125}Co_{0.125}Mn_{0.52}Sn_{0.03}O_2$, which was denoted as CALR.

2.2 Characterization

The morphology was acquired by scanning electron microscopy (SEM, JEOL 6701, Japan). Cross-sectional analysis was prepared by a focused-ion beam microscope (Helios NanoLab 600i, FEI, USA). High-resolution transmission microscopy images (HR-TEM) were acquired by JEM-2100F (JEOL, Japan) operated at 200 kV. Raman spectra were conducted on a DXR Raman microscope (Thermo Scientific, USA) with the laser wavelength of 532 nm. X-ray diffraction (XRD) patterns were collected using a Bruker D8 Advance diffractometer (Germany) equipped with a Cu Kα radiation source ($\lambda1$=1.54060 Å, $\lambda2$=1.54439 Å), the patterns were refined using the Rietveld method and the TOPAS software. X-ray photoelectron spectroscopy (XPS) was performed on Thermo Scientific ESCALab 250Xi (USA) using 200 W monochromatic Al Kα radiation.

2.3 Electrochemical measurements

All the electrochemical tests were conducted using 2032 coin cells assembled in an argon-filled glovebox using lithium metal as anode, Celgard 2300 as separator and 1 M $LiPF_6$ in ethylenecarbonate (EC)/dimethylcarbonate (DMC)/diethylcarbonate (DEC) (1:1:1 in volume ratio) as electrolyte. The cathode electrode was prepared by casting a mixture of active powder, Super P carbon and poly(vinyl difluoride) (PVDF) at a weight ratio of 80:10:10 onto Al foil and then dried at 80 °C in vacuum overnight. The loading of active material was about 4–5 mg cm^{-2}. Galvanostatic charge-discharge was performed using a LAND system over a voltage range of 2–4.7 V and 250 mA g^{-1} for 1 C. Cyclic voltammetry (CV) was carried out using an Autolab PG302N workstation at a scan rate of 0.05 mV s^{-1}, electrochemical impedance spectroscopy (EIS) was also carried out on Autolab with frequency range from 100 kHz to 100 mHz.

3 Results and discussion

The morphology and cross-sectional morphology of PLR and CALR are demonstrated in Figure 1. Both of them consist of spherical secondary particles with diameter about 10–12 μm, of which the distribution is uniform (Figure S1, Supporting Information online), whereas the primary particles differ from each other in size and shape. CO_2 releasing during the sintering of carbonate precursor causes the inside voids, while the second heat treatment densifies the secondary particles with the tap density increasing from 2.0 to 2.2 g cm^{-3}. It is quite interesting that adding minor metal salt affects the configuration of grains, which would be unlikely the consequence of the re-calcination due to the fact that it usually makes the grain grow [23]. The similar change on primary particles occurs when adding other metal chloride such as $AlCl_3$, $CrCl_3$, $FeCl_3$ and $MgCl_2$, as shown in Figure S2, while blurred boundary between primary particles is demonstrated in powders treated with metal hydroxide and isolated particles with large spacing between each other are shown in the samples treated with metal nitrate (Figure S3).

In order to determine the bulk crystal structure, the XRD was carried out, as demonstrated in Figure 2(a, b). The patterns reveal that CALR treated by this strategy still maintains the layered structure with $R\bar{3}m$ space group, the peaks within 2θ range from 20° to 25° correspond to Li/Mn ordering super-lattice of Li_2MnO_3 phase [28,29]. The rietveld refinements were conducted utilizing space group $R\bar{3}m$ with higher symmetry to calculate the atom occupation and structural parameter with results presented in Tables S1 and S2 (Supporting Information online) [28,30]. The parameter c increased upon tin doping owing to its larger ionic radius (112 pm) than Ni, Co and Mn (69, 61 and 53 pm respectively), but the parameter a kept nearly constant which may be a sign of shortened bond between transition metal and oxygen. In addition, the doping amount applied here had little influence on the cation mixing extent, according with previous reports about cation doping [27,31].

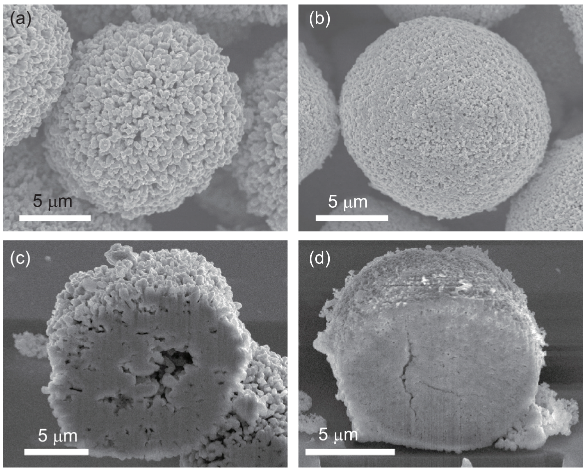

Figure 1 SEM images of (a) PLR and (b) CALR; cross-sectional SEM images of (c) PLR and (d) CALR.

Considering the possible difference between the surface and the bulk structure, Raman spectroscopy are given in Figure 2(c). Two major band at 486 and 601 cm^{-1} are attributed to vibrations involving M–O stretching (A_{1g}) and O–M–O bending (E_g) of layered oxides $LiMO_2$ [32]. And the blue shift of the vibrations could further confirm the shortened bond between transition metal and oxygen. The details on the surface of CALR were further visually demonstrated by HRTEM (Figure 2(d)). Fine layered structure with interplanar distance of 4.7 Å corresponds to the d-spacing of the (003) plane. These results indicate that CALR maintains the layered structure after the treatment on both cation sites and anion sites.

In order to further analyze the bonding and the surface component of the material, XPS was introduced as shown in Figure 3. For O1s core spectra (Figure 3(a)), the peaks at approximately 529 and 532.5 eV correspond to O^{2-} anions in the crystalline network and by-product Li_2CO_3 on surface resulting from the storage instability of Li-rich materials [19,21]. It is worth noting that the elevated binding energy of lattice O indicates the intensified interaction between oxygen and the metal, which is in coincidence with the variation in the lattice parameter and Raman shift. The novelty comes from the intensified peak at around 531 eV (painted green) indicating the hybridization of M3d-O2p, of which enhancement facilitates the participation of electrons localized close to p orbital to form O_2^{2-} providing reversible anodic redox [18,33]. In addition, the hybridization enhancement can also improve the structural stability upon oxygen oxidation during the extended activation plateau. The increase of the satellite peak of $Ni2p_{3/2}$ core spectra is another evidence of such intensification (Figure 3(b)) [34]. Upon chloride species detaching from the lattice of the layered structure during the second calcination by force of thermodynamics, transition metal ions are oxidized to compensate the charge balance, which is confirmed by the rise of Ni binding energy. The oxidization reduces the proportion of c3d^{9}L state and improves the O2p hybridization with transition metal 3d states as a consequence [30,34].

On behalf of clarifying the process of the treatment, we also ran XPS on samples without the rinse and reheating procedure (denoted as CLR). The $Sn3d_{5/2}$ core spectra (Figure 3(c)) clearly demonstrate that Sn ions successfully enter the lattice instead of adhering to the surface and they still maintain

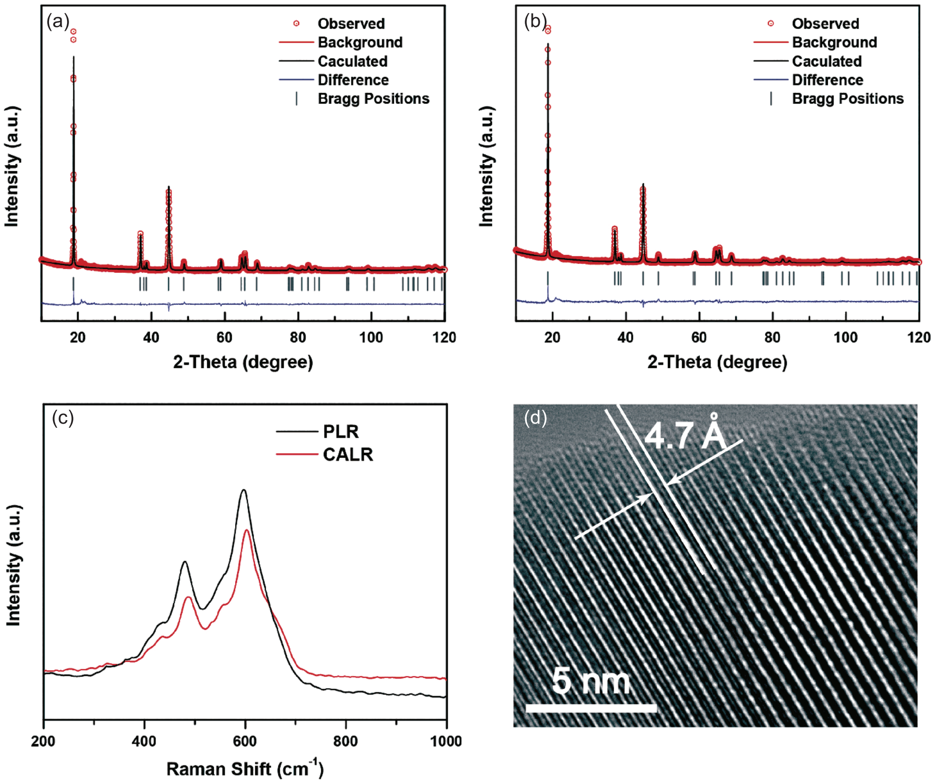

Figure 2 Powder XRD pattern and Rietveld refinement plots of (a) PLR and (b) CALR; (c) Raman spectra obtained for PLR and CALR; (d) HR-TEM image of (003) crystal planes in CALR (color online).

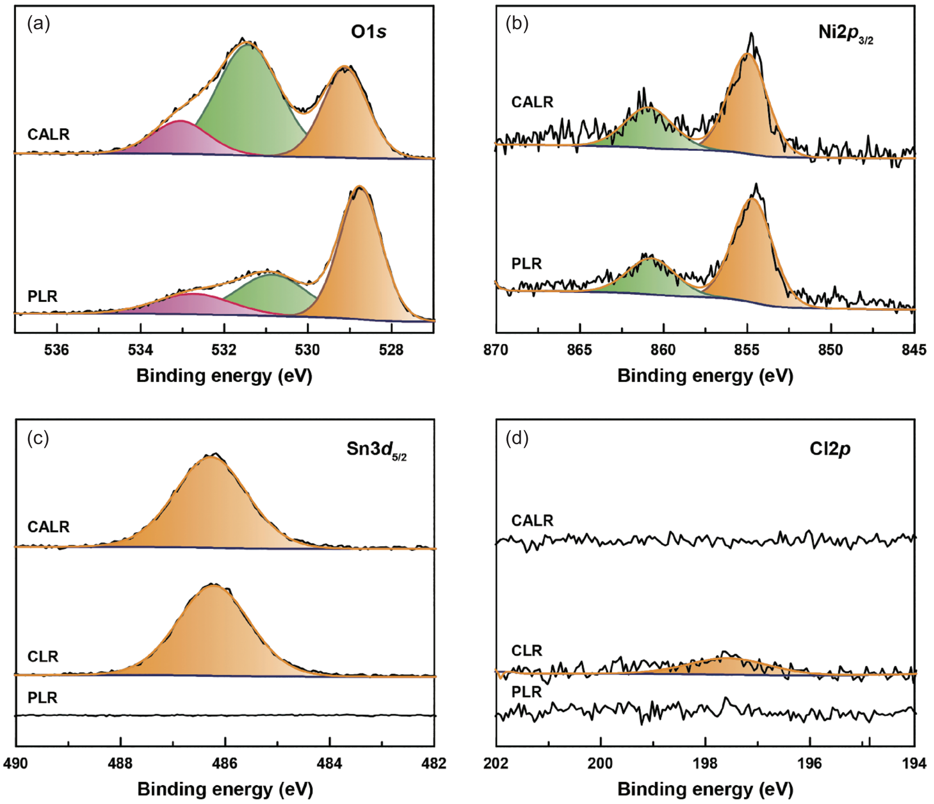

Figure 3 XPS core peaks of (a) O1s, (b) $Ni2p_{3/2}$, (c) $Sn3d_{5/2}$ and (d) Cl2p. The annotation CLR refers to samples treated just with the first calcination (color online).

bivalent with binding energy of 486.2 eV through two-step calcination. As for the Cl2p spectra shown in Figure 3(d), the binding energy of chloride bonded to the structure in CLR is 197.5 eV, even weaker than that of thermolabile ammonium chlorides (197.9 eV). It also indicates the absence of chloride in CALR. The heat applied in the second calcination removes all of chloride species and thus slightly increase valence of transition metal. It is a remarkable fact that the Cl is totally expelled since its coordination effect may corrode the current collector Al foil and further deteriorate the performance of the battery [35,36]. In general the approach reported here penetrates spectator ions with large ionic radius such as Sn^{2+} and weakly bonded chloride anions into the layered lattice in the first step sintering with stannous chloride, and then expel the latter species by the second calcination which leads to slightly valance elevation of transition metal and more importantly the increase of O2p hybridization with transition metal 3d states.

The electrochemical performances of PLR and CALR are displayed in Figure 4. Our focus is on the electrochemical activation plateau at approximately 4.5 V, which is related to the oxygen loss and anodic redox participation [2,14,16]. When charged at 0.05 C (1 C=250 mA g^{-1}) from 2.0 to 4.7 V (Figure 4(a)), the initial charge capacities of PLR and CALR are 340 and 372 mA h g^{-1}, respectively. Assuming the charge capacity below 4.45 V belongs to oxidation of $Ni^{2+}\rightarrow Ni^{4+}$ and $Co^{3+}\rightarrow Co^{4+}$ in $LiMO_2$, regardless of the difference in polarization, the capacity involved with oxygen anions increases from 207 to 225 mA h g^{-1} after the modification [31,37]. The increase in capacity of plateau region in charging can not cover all the discharge capacity increase owing to kinetic enhancement caused by large Sn^{2+} doping, which will be discussed latterly. To confirm the intensification of anodic participation, XPS on the electrodes at fully charged state was conducted with the O1s spectra shown in Figure S4. Compared to the results of uncycled powders, additional peaks at 530.5 eV are assigned to existence of O_2^{n-} species or uncoordinated oxygen atoms, as discussed in previous reports [18,19,24]. The CALR electrode generates more peroxo-like species than PLR electrode, coinciding with the extended charge plateau. The elevated anodic redox participation fully activates Li-rich material to totally offer discharge capacity of 282 mA h g^{-1}. Similar scenario occurs when cycled at 0.2 C (Figure S5(a)). And the differential capacity plot clearly demonstrates the intensified $O^{2-}\rightarrow O_2^{n-}$ reaction and reduced voltage hysteresis of this reaction (Figure S5(b)). In addition, the sluggish reaction kinetics in the plateau region aggravates incomplete activation in the first cycle at high current density [31,38,39]. As a result, the discharge capacity of CALR is 251 mA h g^{-1} at the first cycle and progressively increases to 258 mA h g^{-1} in three cycles (Figure 4(b)). Though comes through the same electrochemical activation of 7 mA h g^{-1}, PLR takes five cycles to complete. All these performance improvements about capacity are attributed to the altered hybridization of M3d-O2p.

Control experiments were conducted to further confirm the conclusion about the effect of expelling chloride. We applied

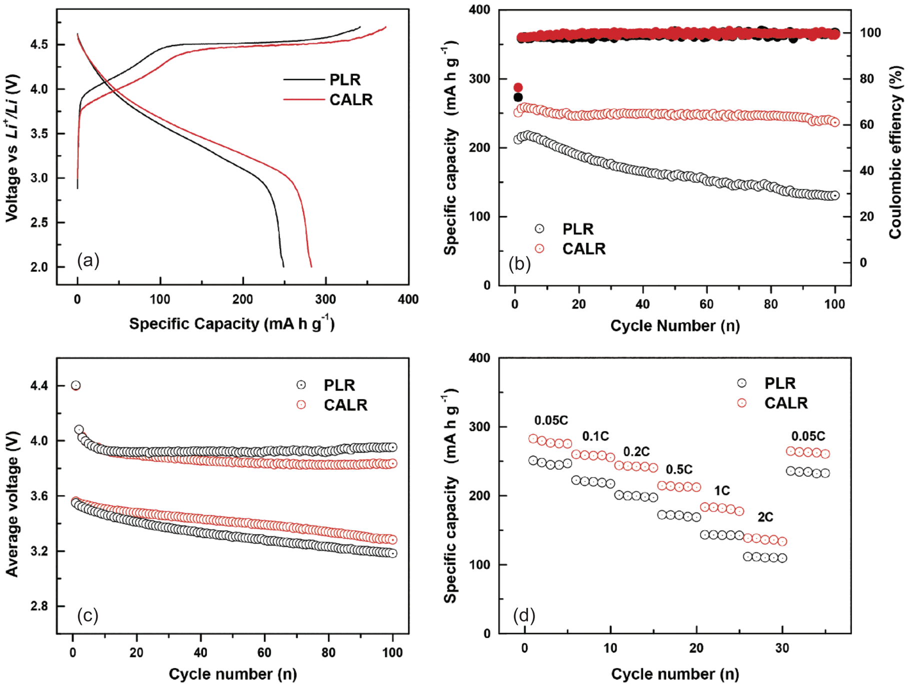

Figure 4 (a) The initial charge-discharge curves of PLR and CALR at 0.05 C; (b) the cycling performance of PLR and CALR; (c) average voltage as a function of cycle numbers for PLR and CALR; (d) rate performance for PLR and CALR (color online).

the same experiment parameter except for substituting $SnCl_2$ with $AlCl_3$, $CrCl_3$, $FeCl_3$, $MgCl_2$, $Al(OH)_3$ or $Al(NO_3)_3$. As expected, prolonged plateau regions were gained in all the samples calcined with metal chloride in spite of variation in transition metal (Figure S6(a)). However, electrochemical performance merely changes when treated with metal hydroxide or nitrate (Figure S6(b)).

Apart from the activated anodic contribution to capacity, the dopants plays an effective role in stability and kinetics, which are demonstrated by the cycling performance and rate performance in Figure 4(b–d). Compared with PLR (59.9% capacity retention after 100 cycles), CALR exhibited excellent cycle stability, with 91.5% capacity retention after 100 cycles. The electro-inactive dopant tin ions act as pillars in supporting the structure and by this means contribute to the stability during prolonged cycling. Moreover, as Sathiya and co-workers [24] suggested, large spectator Sn^{2+} ions help with slowing down the tetrahedral position trapping, which is the origin of voltage decay, leading to a stabilized average discharge voltage with just 0.279 V faded after 100 cycles at 0.2 C. The reduction peak shift in the cyclic voltammograms (CV) monitored in Figure 5(a, b) proves the mitigated voltage decay at the same time [40]. On the other hand, the expanded lattice parameter *c* facilitates the Li^+ diffusion and endows better rate performance to CALR (Figure 4(d)). We redrew the plot of rate performance with normalization capacity replacing the specific discharge capacity so as to rule out underlying factors of the anodic participation (Figure S7), in which CALR still row over PLR. To better understand the dynamic characters of each electrode, the electrochemical impedance spectroscopy (EIS) at open circuit was conducted with results shown in Figure 5(c). Compared with PLR electrode, CALR electrode shows lower charge transfer resistance which might be beneficial to its rate performance (Table S3, Supporting Information online) [31,41]. Though discussed separately, anion hybridization intensification and cation doping synergistically cooperate to gain such achievements. Taking the stability for an example, Sn ions alleviate the phase transformation, in the meantime, the hybridization strengthens the bond and provides improved structural stability upon anodic redox [24,30,34,38].

4 Conclusions

In summary, we have prepared performance enhanced Li-rich material with simultaneous modification on both of the cation

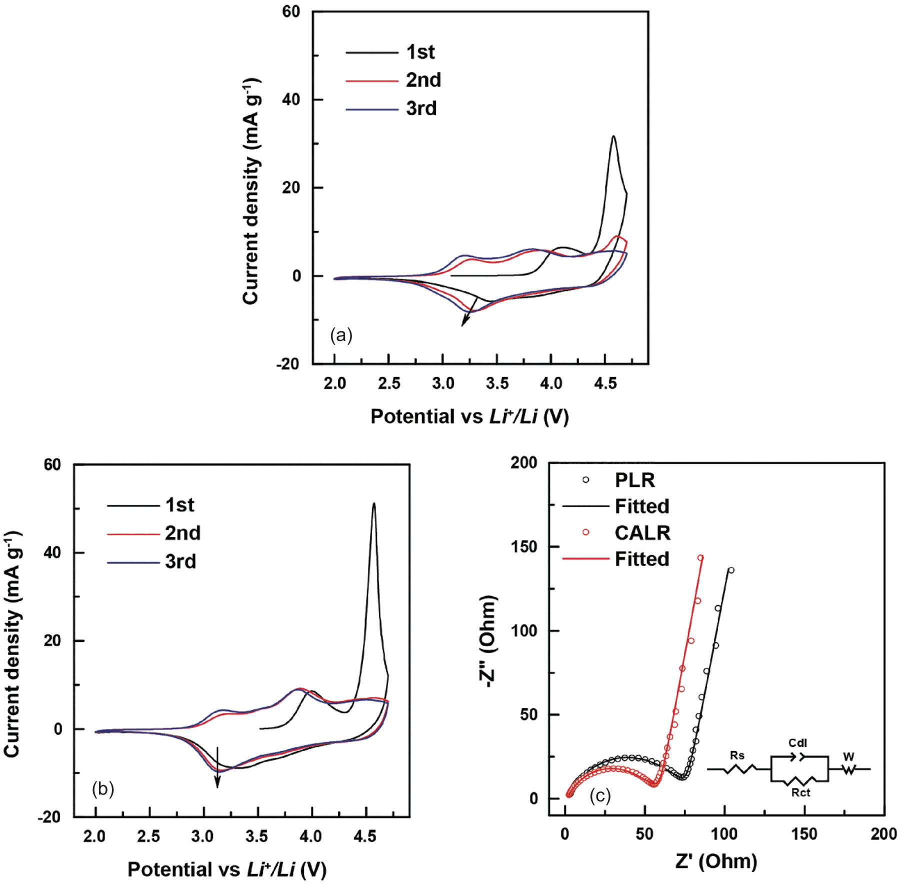

Figure 5 Cyclic voltammograms of (a) PLR electrode and (b) CALR at a scan rate of 0.05 mV s^{-1}; (c) electrochemical impedance spectra (EIS) of the PLR and CALR electrodes at open circuit (color online).

and anion sites via calcination with transition metal chloride and then washing-reheating. The first sintering leaves spectator Sn^{2+} ions and weakly bonded chloride species, which are expelled upon the second one accompanied with elevated hybridization between transition metal 3d and oxygen 2p orbitals. The d-p hybridization facilitates anionic ($O^{2-} \rightarrow O_2^{2-}$) reversible redox process, meanwhile the dopants effectively obviates the phase transition and enlarges the channel for Li^+ diffusion. Their intimately cooperation endows Li-rich materials with high specific capacity at various current density and structural stability during constantly charging and discharging. To be specific, the modified material delivers a specific capacity of 282 mA h g^{-1} at 0.05 C, 258 mA h g^{-1} at 0.2 C with 90.2% retention and 0.279 V decay of the average discharge after 100 cycles. More importantly, not just specific stannous chloride but a series of metal chloride share the same activation in anodic redox participation. This strategy not only provides a simple and effective way to take advantage of anodic redox on the foundation of stability in Li-rich materials, but also demonstrates the possibility of tuning doped cation with proper energy levels and ionic radius to achieve better electrochemical and physical properties.

Acknowledgments This work was supported by the National Key R&D Program of China (2016YFA0202500), the National Natural Science Foundation of China (51225204, 21127901), and the "Strategic Priority Research Program" of the Chinese Academy of Sciences (XDA09010100).

Conflict of interest The authors declare that they have no conflict of interest.

1 Goodenough JB, Park KS. *J Am Chem Soc*, 2013, 135: 1167–1176
2 Seo DH, Lee J, Urban A, Malik R, Kang SY, Ceder G. *Nat Chem*, 2016, 8: 692–697
3 Xin S, Chang ZW, Zhang XB, Guo YG. *Natl Sci Rev*, 2017, 4: 54–70
4 Dunn B, Kamath H, Tarascon JM. *Science*, 2011, 334: 928–935
5 Whittingham MS. *Chem Rev*, 2004, 104: 4271–4302
6 Liu W, Oh P, Liu X, Lee MJ, Cho W, Chae S, Kim Y, Cho J. *Angew Chem Int Ed*, 2015, 54: 4440–4457
7 Freire M, Kosova NV, Jordy C, Chateigner D, Lebedev OI, Maignan A, Pralong V. *Nat Mater*, 2016, 15: 173–177
8 Lu Z, MacNeil DD, Dahn JR. *Electrochem Solid-State Lett*, 2001, 4: A191
9 Thackeray MM, Johnson CS, Vaughey JT, Li N, Hackney SA. *J Mater Chem*, 2005, 15: 2257–2267
10 Yu H, Ishikawa R, So YG, Shibata N, Kudo T, Zhou H, Ikuhara Y. *Angew Chem Int Ed*, 2013, 52: 5969–5973
11 Gu L, Xiao D, Hu YS, Li H, Ikuhara Y. *Adv Mater*, 2015, 27: 2134–2149
12 Long BR, Croy JR, Dogan F, Suchomel MR, Key B, Wen J, Miller DJ, Thackeray MM, Balasubramanian M. *Chem Mater*, 2014, 26: 3565–3572
13 Armstrong AR, Holzapfel M, Novak P, Johnson CS, Kang SH, Thackeray MM, Bruce PG. *J Am Chem Soc*, 2006, 128: 8694–8698
14 Tran N, Croguennec L, Ménétrier M, Weill F, Biensan P, Jordy C, Delmas C. *Chem Mater*, 2008, 20: 4815–4825
15 Yabuuchi N, Yoshii K, Myung ST, Nakai I, Komaba S. *J Am Chem Soc*, 2011, 133: 4404–4419
16 Xu B, Fell CR, Chi M, Meng YS. *Energ Environ Sci*, 2011, 4: 2223–2233
17 Luo K, Roberts MR, Hao R, Guerrini N, Pickup DM, Liu YS, Edström K, Guo J, Chadwick AV, Duda LC, Bruce PG. *Nat Chem*, 2016, 8: 684–691
18 Sathiya M, Rousse G, Ramesha K, Laisa CP, Vezin H, Sougrati MT, Doublet ML, Foix D, Gonbeau D, Walker W, Prakash AS, Ben Hassine M, Dupont L, Tarascon JM. *Nat Mater*, 2013, 12: 827–835
19 Foix D, Sathiya M, McCalla E, Tarascon JM, Gonbeau D. *J Phys Chem C*, 2016, 120: 862–874
20 Luo K, Roberts MR, Guerrini N, Tapia-Ruiz N, Hao R, Massel F, Pickup DM, Ramos S, Liu YS, Guo J, Chadwick AV, Duda LC, Bruce PG. *J Am Chem Soc*, 2016, 138: 11211–11218
21 Qiu B, Zhang M, Wu L, Wang J, Xia Y, Qian D, Liu H, Hy S, Chen Y, An K, Zhu Y, Liu Z, Meng YS. *Nat Commun*, 2016, 7: 12108
22 Chen CJ, Pang WK, Mori T, Peterson VK, Sharma N, Lee PH, Wu SH, Wang CC, Song YF, Liu RS. *J Am Chem Soc*, 2016, 138: 8824–8833
23 Zheng F, Yang C, Xiong X, Xiong J, Hu R, Chen Y, Liu M. *Angew Chem Int Ed*, 2015, 54: 13058–13062
24 Sathiya M, Abakumov AM, Foix D, Rousse G, Ramesha K, Saubanère M, Doublet ML, Vezin H, Laisa CP, Prakash AS, Gonbeau D, VanTendeloo G, Tarascon JM. *Nat Mater*, 2015, 14: 230–238
25 Wei W, Chen L, Pan A, Ivey DG. *Nano Energy*, 2016, 30: 580–602
26 Oh P, Ko M, Myeong S, Kim Y, Cho J. *Adv Energ Mater*, 2014, 4: 1400631
27 Wang PF, You Y, Yin YX, Wang YS, Wan LJ, Gu L, Guo YG. *Angew Chem Int Ed*, 2016, 55: 7445–7449
28 Muhammad S, Kim H, Kim Y, Kim D, Song JH, Yoon J, Park JH, Ahn SJ, Kang SH, Thackeray MM, Yoon WS. *Nano Energy*, 2016, 21: 172–184
29 Zhang J, Guo X, Yao S, Qiu X. *Sci China Chem*, 2016, 59: 1479–1485
30 Shi JL, Zhang JN, He M, Zhang XD, Yin YX, Li H, Guo YG, Gu L, Wan LJ. *ACS Appl Mater Interfaces*, 2016, 8: 20138–20146
31 Qing RP, Shi JL, Xiao DD, Zhang XD, Yin YX, Zhai YB, Gu L, Guo YG. *Adv Energ Mater*, 2016, 6: 1501914
32 Deng YP, Fu F, Wu ZG, Yin ZW, Zhang T, Li JT, Huang L, Sun SG. *J Mater Chem A*, 2016, 4: 257–263
33 de Groot FMF, Grioni M, Fuggle JC, Ghijsen J, Sawatzky GA, Petersen H. *Phys Rev B*, 1989, 40: 5715–5723
34 Nesbitt HW, Legrand D, Bancroft GM. *Phys Chem Miner*, 2000, 27: 357–366
35 Kühnel RS, Balducci A. *J Power Sources*, 2014, 249: 163–171
36 Tong Z, Tian Y, Zhang H, Li X, Ji J, Qu H, Li N, Zhao J, Li Y. *Sci China Chem*, 2017, 60: 13–37
37 Schipper F, Erickson EM, Erk C, Shin JY, Chesneau FF, Aurbach D. *J Electrochem Soc*, 2017, 164: A6220–A6228
38 Wang Y, Yang Z, Qian Y, Gu L, Zhou H. *Adv Mater*, 2015, 27: 3915–3920
39 Yu X, Lyu Y, Gu L, Wu H, Bak SM, Zhou Y, Amine K, Ehrlich SN, Li H, Nam KW, Yang XQ. *Adv Energ Mater*, 2014, 4: 1300950
40 Shi JL, Xiao DD, Zhang XD, Yin YX, Guo YG, Gu L, Wan LJ. *Nano Res*, 2017, 1–9
41 Wang JL, Luo H, Mai YJ, Zhao XY, Zhang LZ. *Sci China Chem*, 2013, 56: 739–745